# Evolution of terahertz waves in air plasma driven by orthogonally polarized two-color pulses

**Ya Bai (白 亚)[1], Jie Tang (唐 杰)[1], Rongjie Xu (许荣杰)[1], and Peng Liu (刘 鹏)[1,2,*]**

[1]*State Key Laboratory of High Field Laser Physics, Shanghai Institute of Optics and Fine Mechanics, Chinese Academy of Sciences, Shanghai 201800, China*

[2]*IFSA Collaborative Innovation Center, Shanghai Jiao Tong University, Shanghai 200240, China*

**Corresponding author: peng@siom.ac.cn*

Received February 22, 2016; accepted June 24, 2016; posted online July 15, 2016

We experimentally investigate the evolution of the terahertz (THz) waveform and polarization state inside the plasma filament produced by orthogonally polarized two-color pulses. We find that the variation of the THz polarization state along the plasma column is dominantly caused by the relative phase difference and spectra blue shift of the two-color field. Elliptically polarized THz radiation is generated by controlling the initial relative phase and the filament length. The result indicates the coherent control of the polarization state of the THz emission.

*OCIS codes: 040.2235, 260.5210, 320.7110, 350.5400.*
*doi: 10.3788/COL201614.093201.*

Intense femtosecond laser pulses undergo filamentation in ambient air, and the induced plasma becomes a unique source of intense broadband terahertz (THz) radiation when driven by the two-color [fundamental ($\omega$) and second harmonic ($2\omega$)] laser pulses[1–13]. The polarization state of the THz radiation, namely the ellipticity and polarization direction, attracts much attention since it provides insights on the mechanism of THz generation in laser filamentation[7–12], and it offers a remotely controllable THz waves that can be applied in the imaging[14–16], spectroscopy[17], dichroism[18], and polarimetry[19,20] in the THz range.

In order to generate the elliptically polarized THz field, the two orthogonal components of the THz waves need to have comparable amplitudes and adjustable phase differences. In previous studies it has been shown that the THz polarization rotates following the phase difference of the two-color pulses, which is due to the tailored laser fields that can manipulate the electron trajectories that determine the emission of THz polarization[7,8]. On the other hand, the ellipticity of the THz emission could not be controlled completely by the means of all-optical laser fields. Recently, You *et al.* has shown that an elliptically polarized THz wave is produced in the far field through the generation of rotating local THz waves and the phase retardance due to the velocity mismatch between the optical pump and THz emission in the generation process[12]. However, the polarization of the THz waves in most experiments is slightly elliptically polarized even when the driving pulses are circularly polarized[8]. The investigation of the THz waves' evolution within the filament is therefore necessary to reveal the mechanism of the generated THz ellipticity.

In this Letter, we measured the evolution of THz waveforms and polarization states within the air plasma when the two-color pulses are orthogonally polarized. As the effective length of the air plasma adjusted, the far-field THz wave varies accordingly. Although the polarization state of the THz waves is mainly linearly polarized and parallel to the polarization of the $2\omega$ pulse at the position where the THz fields experience polarity inversion, the THz waves with large ellipticities are observed as a consequence, while the filament length is short enough to neglect the velocity mismatch effect between the optical pump and the THz emission. Our analysis indicates that the varying phase and spectra blue shift of the propagating two-color pulses can not only produce the rotating local THz waves, but also induce a phase difference between the orthogonal polarization components. This provides a way to manipulate the ellipticity of THz emissions by controlling the initial phase difference of the laser fields and the effective plasma length.

Experiments were carried out using a Ti:sapphire amplifier laser system which produces pulses with the duration of 40 fs in full width at half-maximum (FWMH), 6.5 mJ per pulse, a center wavelength of 800 nm with a 1 kHz repetition rate. The laser pulse was split into a pump pulse and a weak probe pulse to generate and detect the THz emission, respectively. The $2\omega$ pulse was generated by passing the $\omega$ pulse through a type-I BBO crystal with a 200 μm thickness, as shown in Fig. 1(a). An inline phase compensator composed of a 4 mm-thick calcite and a pair of fused silica wedges were employed to fine tune the phase delay between the $\omega$ and $2\omega$ pulses. Both of the $\omega$ and $2\omega$ pulses are linearly polarized with orthogonal polarizations, and the ellipticity is around 1/240 in terms of pulse energy. Here we define the polarization direction of the $\omega(2\omega)$ pulse as the $x(y)$ axis, representing $p(s)$ polarization. The combined $\omega$ and $2\omega$ pulse were focused in air by a plano-convex lens $f = 300$ mm, with the pulse energy of 650 and 100 μJ for the $\omega$ and $2\omega$ pulses, respectively. A plasma column of about 14 mm in length was created at the focal region.

 

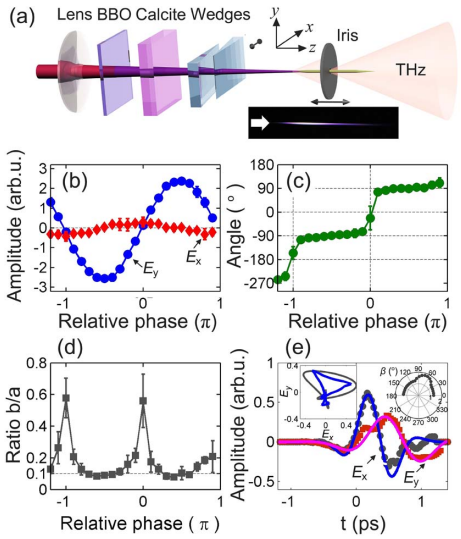


Fig. 1. (a) Schematic of the experimental setup. Below: Image of the filament fluorescence record by a CCD camera. (b) The $x$ and $y$ components of the generated THz amplitude. (c) The polarization angle and (d) the ellipticity expressed as the ratio $b/a$ versus the phase delay of the two-color pulses. In (c)–(d) each point is an average of four groups of data, and the error bars show the rms error. (e) Measured THz wave components for the relative phase $\theta_0 = 0$ (in black and red dots), and the THz wave fitted by the subcycle pulse expression (in blue and pink lines). Inset, left: temporal evolution of THz field of the experimental data (blue line), and the fitted results (black line); right: the calculated angle-resolved THz power distribution of the measured results.

The emitted THz waves were collimated and refocused by a pair of parabolic mirrors (2 in diameter, focus length $f_1 = 3$ in, $f_2 = 2$ in, respectively), and measured by the electro-optic (EO) sampling technique with a 1 mm-thick ZnTe crystal. To characterize the polarization state of the THz waves, a pair of wire grid polarizers (THz HDPE polarizer, TYDEX, with contrast >99.5% below 10 THz) were used. The alignment of the two polarizers is similar to the setup reported in Ref. [21]. The collimated THz beam first passes through a rotatable polarizer (Pola.1) that transmits 0° or 45° polarized THz components relative to the $y$ axis ($s$ polarization), then passes through the second polarizer (Pola.2) at a fixed angle that only transmits an $s$ polarized THz wave to ensure the identical EO detection efficiency for the two components. The $x$ and $y$ polarized THz components were reconstructed by analyzing the measured 0° and 45° polarized waves.

First, in order to demonstrate the dependence of the THz emission on the relative phase of the two-color pulses, we measured the $x$ and $y$ components of the THz waveforms while inserting the wedges. The THz amplitude as a function of the relative phase is shown in Fig. 1(b). As one can see, the maximum amplitude of the $x$ component shifted by $\pi/2$ in advance in comparing it with the $y$ component, and the maximum value of the $x$ component is only one-sixth of that of the $y$ component, which is consistent with the results reported in Ref. [11].

For the purpose of describing the polarization property of the THz emission, we extract the polarization angle and ellipticity. The measured elliptically polarized THz field can be expressed as $\boldsymbol{E}_{\mathrm{THz}}(t) = E_x(t)\hat{e}_x + E_y(t)\hat{e}_y$, which makes it simple to find the maximum and minimum amplitude, expressed as $|\boldsymbol{E}_{\mathrm{THz}}(t)|_{\max}$ and $|\boldsymbol{E}_{\mathrm{THz}}(t)|_{\min}$, respectively. The polarization angle, $\psi$, is defined as the direction of $|\boldsymbol{E}_{\mathrm{THz}}(t)|_{\max}$, and the ellipticity is expressed as the ratio $b/a = |\boldsymbol{E}_{\mathrm{THz}}(t)|_{\min}/|\boldsymbol{E}_{\mathrm{THz}}(t)|_{\max}$. However, for the sake of accuracy, the ratio was extracted by calculating the projection of the THz electric field on an imaginary polarizer that was continuously rotating in the $x$–$y$ plane; the angular distribution of the THz power could be obtained in $P_{\mathrm{THz}}(\alpha) = \sum |\boldsymbol{E}_{\mathrm{THz}}(t)\cos(\alpha - \beta)|^2 \mathrm{d}t$, where $\alpha$ is the angle between the polarization direction of the imaginary polarizer and the $x$ axis, and $\beta$ is the angle between the THz field vector and the $x$ axis. The ratio is defined as $b/a = (P^{\min}_{\mathrm{THz}}/P^{\max}_{\mathrm{THz}})^{1/2}$, where $P^{\max}_{\mathrm{THz}}$ is the maximum power, and $P^{\min}_{\mathrm{THz}}$ is the minimum power.

As the relative phase varied from $0.2\pi$ to $0.8\pi$, the nearly linear THz polarization was obtained with the ellipticity $b/a \approx 0.1$ as the polarization angle changed from 83°–103°. While for relative phase between $-0.2\pi$ and $0.2\pi$, the THz field is elliptically polarized with the largest value of $b/a = 0.6$, and the polarization angle changes by 164°, which indicates the reversal of the THz field polarity [shown in Figs. 1(c) and 1(d)].

For the critical data at the relative phase $\theta_0 = 0$, the THz wave was observed with the highest ellipticity, while the large variation of the polarization angle and ellipticity may arise from the long-term instability in multiple measurements. The inset of Fig. 1(e) shows the temporal evolution of the THz field vector for the relative phase $\theta_0 = 0$, the phase difference between the $x$ and $y$ components is $0.55\pi$ for a 1 THz frequency (despite relatively large fluctuations across the THz spectral range, i.e., 0.3–3 THz).

In order to eliminate the instability in the measurements, we fitted the THz waves using the subcycle pulse expression based on the complex-source model proposed by Lin *et al.*[22]. The THz field is radiated from oscillating dipole moment in which we take a Gaussian envelope for simplicity, written as

$$E(t) = \mathrm{Re}[-iE_0 \exp(-\tau^2/2T^2)\exp(i\varphi(\tau))], \qquad (1)$$

where $\varphi(\tau) = \omega_0\tau + 2\,\mathrm{atan}[\mathrm{sgn}(\tau)\sqrt{1+\alpha^2} - \alpha] + \varphi_0 - \pi/2$ is the temporal phase, $\alpha = (1 + \omega_0^2 T^2 - \tau^2/T^2)/2\omega_0\tau$, $\omega_0 = 2\pi f_0$ is the carrier wave frequency, and $2\sqrt{2\ln 2}\,T$ is the FWHM of the Gaussian envelope. The parameters are chosen to best fit the measured temporal THz field, as shown in Fig. 1(e). The resulting electric field strengths are $E_{0,x} = 0.64$ and $E_{0,y} = 0.34$ in arbitrary units, the oscillator frequencies are $f_{0,x} = 0.67$ THz and $f_{0,y} = 0.5$ THz, the pulse durations are $T_x = 0.32$ ps and $T_y = 0.5$ ps, and the absolute phases are $\varphi_x = 0.8\pi$ and $\varphi_y = 0.8\pi$, for the $x$ and $y$ components, respectively. The fitted results revealed the temporal THz field vector

with a right handed elliptical polarization [inset of Fig. 1(e)].

Although the THz field is not perfect elliptically polarized due to the subcycle nature of the THz waveform, the calculated polar angle-resolved THz power distribution of the measured wave reveals that the THz emission is close to being circularly polarized [shown in the inset of Fig. 1(e)] with the ratio $b/a = 0.7$.

For probing the THz generation dynamics within the air plasma, we apply an iris of a 0.5 mm inner aperture along the plasma column concentric with the propagation axis of the pump pulses. As a result, the THz emitted from filament segment before the aperture was blocked, while the THz is generated from the filament segment after the aperture was collected into the EO sampling setup. As indicated in a previous publication, a small aperture may affect the background energy reservoir surrounding the filament core and cease the plasma formation[23]. We check this effect by placing the iris at the beginning of the filament; the measured THz wave shows no significant difference compared to the case without the iris, and the fluorescence image also shows no difference under the two conditions.

By scanning the iris along the laser propagation direction in a step size of 0.375 mm, the THz emission constructed from various plasma positions was recorded and shown in the map of Fig. 2(a) for the initial relative phase of $\theta_0 = -0.5\pi$. The THz waves emitted from the tail of the filament show an opposite polarity compared to that from a 14 mm-long filament. Obviously, the amplitude modulation of the THz field indicates a polarity inversion for a 6.5 mm-long filament, as shown in Fig. 2(b). The polarization state of the THz emission is mainly linear and parallel to the $y$ axis. Nevertheless, the elliptically polarized THz wave was observed for the filament length from 6–8 mm, with its maximum ellipticity reaching to $b/a = 0.22$.

We note that the measured far-field THz radiation is the integration of the THz emission from the unblocked filament. The spatially resolved THz emission can be retrieved by taking the differentiation of the measured THz waves, which is plotted in Figs. 3(a) and 3(b). The amplitude of the THz waves modulated from a negative to a positive polarity as the filament length increased, and the polarity inversion positions shift from $z = -0.5$ mm to $z = -3$ mm as the initial relative phase changed from $\theta_0 = -0.5\pi$ to $\theta_0 = 0$.

The waveforms in Figs. 3(a) and 3(b) show a gradual spectra phase variation as it changed from a positive to a negative polarity, which is responsible for the generation of an elliptically polarized THz wave. Such phenomenon may originate from two effects: the relative phase shift of the two-color pulses, and the nonlinear propagation induced blue shift of the pump frequencies[5]. The relative phase shift includes the linear and nonlinear dispersion induced phase variation and the Gouy phase shift, which can lead to the rotation of the polarization direction of the plasma current[24,25]. The blue shift of the pump spectra is due to a plasma induced refractive index change from the optical field ionization process, which depends on plasma density and nonlinear propagation distance[5,26,27]. According to Ref. [6], the emitted THz spectrum has a simplified expression $E_{\mathrm{THz}}(\omega) \propto \sum C_n e^{i\omega t_n}$, where $e^{i\omega t_n}$ is the spectral phase of the THz emission from each ionization event, $t_n$. The blue shift of the pump pulse can affect the ionization event and reshape the local THz spectra amplitude and phase as a consequence. This inherent spectra phase is dependent on the relative phase changes of the pump pulses.

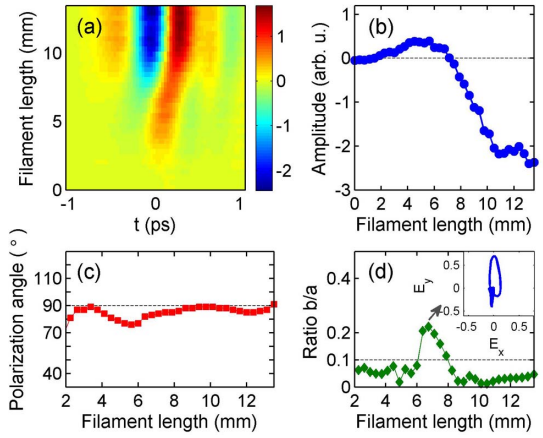


Fig. 2. (a) Measured THz waveforms as the filament length increased for the initial relative phase $\theta_0 = -0.5\pi$, the colorbar shows the amplitude of the THz waves. (b) Modulation of the THz amplitude as the function of the filament length, taken from (a) at the delay time of 0 ps. (c) Polarization angle and (d) ellipticity of the constructed THz field versus the filament length. Inset shows the temporal evolution of the THz field for 6.5 mm-long filament.

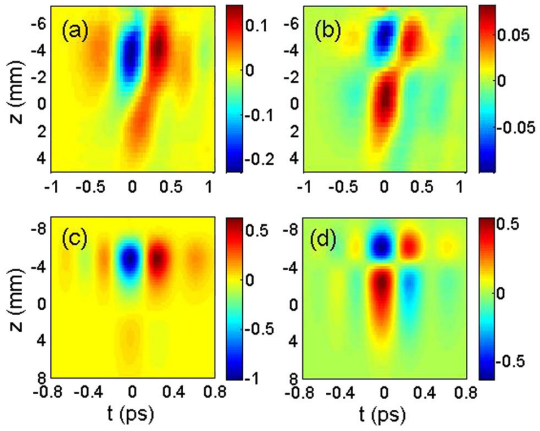


Fig. 3. THz waves generated from each section of the filament by differentiating the measured THz waves for the initial relative phases (a) $\theta_0 = -0.5\pi$ and (b) $\theta_0 = 0$, respectively; the calculated THz waves at the filament positions for the different initial relative phases (c) $\theta_0 = -0.3\pi$ and (d) $\theta_0 = 0.2\pi$, respectively. The color bar shows the amplitude of the THz waves.

It is noteworthy that the retardance effect stressed by You *et al.* is response for elliptically polarized THz emission as the filament is longer than the dephasing length of the two-color pulses[12]. The phase retardance of the THz wave is caused by the velocity mismatch between the optical pump and the THz wave. Expressed by Eq. (4) in Ref. [12], the accumulation of phase difference is proportional to the refractive index difference and filament length. For example, if the refractive index difference is $\Delta n = n_{\rm opt} - n_{\rm THz} = 7 \times 10^{-3}$, and filament length is 10 mm, the maximum phase difference is only $0.05\pi$ for 1 THz of frequency, which is not enough to explain the THz ellipticity observed in our experiments.

In order to simulate the modulation of the THz field in a plasma filament, we consider the transient photocurrent model[3,4], including the nonlinear propagation effects of two-color pulses in transparent media[5]. For simplicity, only the on-axis two-color laser field is considered in the propagation coordinate, expressed as

$$\begin{cases} \boldsymbol{E}_x(z,t) = E^x_{\rm env}(z,t) \cdot \exp[-i(\omega_0 t - \phi_x(z))] \\ \boldsymbol{E}_y(z,t) = E^y_{\rm env}(z,t) \cdot \exp[-i(2\omega_0 t - \phi_y(z))], \end{cases} \quad (2)$$

where $E^x_{\rm env}(z,t)$ and $E^y_{\rm env}(z,t)$ represents the Gaussian envelope in the spatial and temporal domains, and $\phi_x(z)$ and $\phi_y(z)$ are the phase retardations for $\omega$ and $2\omega$, respectively. In the calculations, we consider a small blue shift of 4 THz for the $\omega$ spectra (original center frequency 375 THz); the maximum intensity of the ω pulse, $I_\omega = 8.5 \times 10^{13}$ W/cm$^2$, is one order of magnitude larger than that of the $2\omega$ pulse, $I_{2\omega} = 0.8 \times 10^{13}$ W/cm$^2$. The resulted maximum electron density is $2.2 \times 10^{16}$ cm$^{-3}$. Therefore, the refractive index changes induced by the Kerr nonlinearity is equal to that induced by the plasma, which is consistent with the condition of the intensity clamping in the filament[23,28,29].

Since the THz field is shown to be sensitively determined by the relative phase of the two-color laser field, we then investigated the various phase shift effects in air plasma, including the linear and nonlinear dispersion induced phase shift and the modified Gouy phase shift[25]. The relative phase of the two-color field changes as $\theta(z) = \phi_y(z) - 2\phi_x(z)$. The carrier phases in the transparent media are expressed as

$$\begin{cases} \phi_x(z) = (\omega_0/c)\int n_{\rm fila}(\omega_0, z){\rm d}z + \phi_{\rm Gouy}(\omega_0, z) \\ \phi_y(z) = (2\omega_0/c)\int n_{\rm fila}(2\omega_0, z){\rm d}z + \phi_{\rm Gouy}(2\omega_0, z), \end{cases} \quad (3)$$

in which the first term $n_{\rm fila}(\omega_0, z)$ is the spatially resolved refractive index $n_{\rm fila}(\omega_0,z) = n_0(\omega_0) + \delta n_{\rm Kerr}(\omega_0,z) + \delta n_{\rm plas}(\omega_0,z)$, $n_0$ is the linear refractive index in air. The second term $\delta n_{\rm Kerr}$ is the refractive index change induced by the Kerr nonlinearity, $\delta n_{\rm Kerr} = n_2 I$, $n_2$ is the nonlinear refractive index, and $I$ is laser intensity. The third term $\delta n_{\rm plas}$ is the refractive index change induced by plasma dispersion, $\delta n_{\rm plas} = -\rho_e/2\rho_{\rm cr}$; $\rho_{\rm cr} = m\varepsilon_0\omega_0^2/e^2$ is the critical plasma density in terms of $\varepsilon_0$ vacuum permittivity, $m$ is the electron mass, and $e$ is the electron charge. The second term on the right hand side is the Gouy phase shift. As indicated in Ref. [25], the Rayleigh length is no longer valid in a plasma filament, hence, the Gouy phase shift is modified due to the nonlinear propagation of the laser pulse. Because of the dynamic competition between the optical Kerr effect and plasma defocusing, the modified Gouy phase shift decreases with a gentle slope in comparison to the Gouy phase shift in the linear focus condition. Here, in our simulation, the plasma filament is simplified as a one-dimensional line source; therefore, the linear Gouy phase shift is considered as a substitution of the modified Gouy phase shift.

The intense linearly polarized $\omega$ pulse can induce birefringence in dispersive media due to the difference in the nonlinear refractive index for the laser field that has orthogonal polarizations through the optical Kerr nonlinearity[30,31]. In consideration of the THz generation, the process is on the timescale of the laser pulse duration, so the nonlinear refractive index is mainly from the contribution of the instantaneous electronic response, and the orientational Ramman contribution is negligible[32]. The nonlinear Kerr refractive index can be written as $n_2^x = (3/8n_0(\omega_0))\chi^{(3)}_{xxxx}(\omega_0,\omega_0,-\omega_0)$, $n_2^y = (3/8n_0(2\omega_0))\chi^{(3)}_{yyxx}(2\omega_0,\omega_0,-\omega_0)$ and for laser pulse polarized along the $x$ and $y$ axis, respectively, here $n_0$ is the linear refractive index in air, $\chi^{(3)}_{xxxx}$ and $\chi^{(3)}_{yyxx}$ are third-order susceptibility tensors with the relation $\chi^{(3)}_{xxxx} \approx 3\chi^{(3)}_{yyxx}$. As a consequence, $n_2^x = 3n_2^y$ with $n_2^x = 7.4 \times 10^{-20}$ cm$^2$/W[32].

Figures 4(a) and 4(b) show various kind of calculated relative phase shifts as the function of the $z$ axis. The total relative phase shift experiences a jump of $1.1\pi$ through the plasma region ($z = -8 - 6$ mm) in which the linear phase shift changed by $0.5\pi$; the other $0.6\pi$ contribution arises from the relative Gouy phase shift. The curve of the Kerr effect induced phase shift has a slower slope than that induced by the plasma and, as well, shows inverse sign. The Kerr effect induced phase shift has the trend to decrease the total relative phase shift while being compensated by the plasma induced phase shift.

The THz wave is emitted from the nonvanishing transient photocurrent that is produced during the tunneling

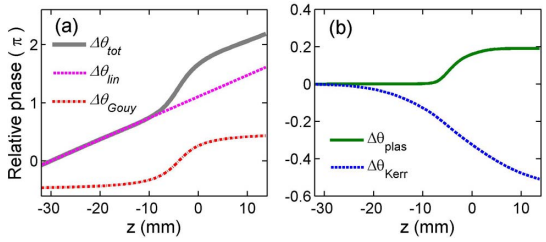


Fig. 4. (a) Total relative phase shift $\Delta\theta_{\rm tot}$ (black solid line), linear phase shift due to the linear refractive index $\Delta\theta_{\rm lin}$ (pink dash line), and phase shift response for the Gouy phase shift $\Delta\theta_{\rm Gouy}$ (real dash line). (b) Phase shift due to the refractive index changes caused by the Kerr nonlinearity $\Delta\theta_{\rm Kerr}$ (blue dash line) and the plasma formation $\Delta\theta_{\rm plas}$ (green solid line).

ionization process[3–5]. The time domain THz field is calculated through the inverse Fourier transform of the calculated spectrum after passing through a low-pass filter <3.4 THz, conforming to the measured spectra range using a 1 mm-thick ZnTe crystal.

In Figs. 3(c) and 3(d), the simulated THz field is plotted as the function of the laser pulse propagation coordinate for two different relative phases, which reproduces the experimental observation as shown in Figs. 3(a) and 3(b).

The calculated THz field is linearly polarized parallel to the $y$ axis, which is consistent with the results for the relative phase from $0.2\pi$ to $0.8\pi$, as depicted in Fig. 1(e). The $x$ component is relatively small due to the vanishing of the photocurrent after a fast oscillation motion of photoelectrons at $\omega$ laser frequencies. While in the experiment, as the THz field polarity reversed, the amplitude of the $y$ component decreased by almost one order of magnitude, and is comparable to the amplitude of $x$ component. Meanwhile, the spectra phase difference of the two components not equal to 0 (or $\pi$), the elliptically polarized THz wave was observed as a consequence.

In addition, the polarization state of the THz wave is relying on the relative phase variations along the filament; therefore, using a higher driven pulse energy to produce a longer filament and gas media with a larger dispersion are beneficial to generate the THz wave with a larger ellipticity.

In conclusion, we discuss the evolution of the THz waveform and polarization states within the air plasma produced by two-color pulses having orthogonal polarizations. The elliptically polarized THz wave is observed at the position where THz waves experience polarity inversion, while close to linearly polarized THz waves can be obtained in most other cases. The demonstration provides useful information for understanding the THz generation process inside the plasma, and enables the polarization states control of the THz emission.

This work was supported by the National Science Foundation of China (Nos. 11274326, 61221064, 61405222, 61505234, 11134010, and 11127901), the Shanghai Sailing Program (No. 14YF1406200), and the National 973 Program of China (No. 2011CB808103).

## References

1. D. J. Cook and R. M. Hochstrasser, Opt. Lett. **25**, 1210 (2000).
2. X. Xie, J. Dai, and X. C. Zhang, Phys. Rev. Lett. **96**, 075005 (2006).
3. K. Y. Kim, J. H. Glownia, A. J. Taylor, and G. Rodriguez, Opt. Express **15**, 4577 (2007).
4. K. Y. Kim, A. J. Taylor, J. H. Glownia, and G. Rodriguez, Nat. Photon. **2**, 605 (2008).
5. I. Babushkin, W. Kuehn, C. Köhler, S. Skupin, L. Bergé, K. Reimann, M. Woerner, J. Herrmann, and T. Elsaesser, Phys. Rev. Lett. **105**, 053903 (2010).
6. I. Babushkin, S. Skupin, A. Husakou, C. Köhler, E. Cabrera-Granado, L. Bergé, and J. Herrmann, New J. Phys. **13**, 123029 (2011).
7. H. Wen and A. M. Lindenberg, Phys. Rev. Lett. **103**, 023902 (2009).
8. J. Dai, N. Karpowicz, and X. C. Zhang, Phys. Rev. Lett. **103**, 023001 (2009).
9. D. Dietze, J. Darmo, S. Roither, A. Pugzlys, J. N. Heyman, and K. Unterrainer, J. Opt. Soc. Am. B **26**, 2016 (2009).
10. Y. Chen, C. Marceau, S. Génier, F. Théberge, M. Châteauneuf, J. Dubois, and S. L. Chin, Opt. Commun. **282**, 4283 (2009).
11. M. Li, W. Li, Y. Shi, P. Lu, H. Pan, and H. Zeng, Appl. Phys. Lett. **101**, 161104 (2012).
12. Y. S. You, T. I. Oh, and K.-Y. Kim, Opt. Lett. **38**, 1034 (2013).
13. J. Zhao, L. Zhang, Y. Luo, T. Wu, C. Zhang, and Y. Zhao, Chin. Opt. Lett. **12**, 083201 (2014).
14. N. C. J. van der Valk, W. A. M. van der Marel, and P. C. M. Planken, Opt. Lett. **30**, 2802 (2005).
15. W. L. Chan, J. Deibel, and D. M. Mittleman, Rep. Prog. Phys. **70**, 1325 (2007).
16. Z. Tan, L. Gu, T. Xu, T. Zhou, and J. Cao, Chin. Opt. Lett. **12**, 070401 (2014).
17. R. Singh, D. K. George, C. Bae, K. A. Niessen, and A. G. Markelz, Photon. Res. **4**, A1 (2016).
18. E. Castro-Camus, J. Lloyd-Hughes, and M. B. Johnston, Appl. Phys. Lett. **86**, 254102 (2005).
19. N. Kanda, K. Konishi, and M. Kuwata-Gonokami, Opt. Express **15**, 11117 (2007).
20. H. Wen, S. N. Pisharody, J. M. Murray, and P. H. Bucksbaum, Phys. Rev. A **73**, 052504 (2006).
21. M. Nagai, N. Mukai, Y. Minowa, M. Ashida, J. Takayanagi, and H. Ohtake, Opt. Lett. **39**, 146 (2014).
22. Q. Lin, J. Zheng, and W. Becker, Phys. Rev. Lett. **97**, 253902 (2006).
23. S. L. Chin, *Femtosecond Laser Filamentation* (Springer, 2010).
24. Y. Liu, A. Houard, M. Durand, B. Prade, and A. Mysyrowicz, Opt. Express **17**, 11480 (2009).
25. Y. Bai, L. Song, R. Xu, C. Li, P. Liu, Z. Zeng, Z. Zhang, H. Lu, R. Li, and Z. Xu, Phys. Rev. Lett. **108**, 255004 (2012).
26. W. M. Wood, C. W. Siders, and M. C. Downer, Phys. Rev. Lett. **67**, 3523 (1991).
27. S. C. Rae and K. Burnett, Phys. Rev. A **46**, 1084 (1992).
28. A. Couairon and A. Mysyrowicz, Phys. Rep. **441**, 47 (2007).
29. J. F. Daigle, A. Jaroń-Becker, S. Hosseini, T. J. Wang, Y. Kamali, G. Roy, A. Becker, and S. L. Chin, Phys. Rev. A **82**, 023405 (2010).
30. P. Béjot, Y. Petit, L. Bonacina, J. Kasparian, M. Moret, and J. P. Wolf, Opt. Express **16**, 7564 (2008).
31. O. Kosareva, N. Panov, V. Makarov, I. Perezhogin, C. Marceau, Y. Chen, S. Yuan, T. Wang, H. Zeng, A. Savel'ev, and S. Leang Chin, Opt. Lett. **35**, 2904 (2010).
32. J. K. Wahlstrand, Y. H. Cheng, and H. M. Milchberg, Phys. Rev. A **85**, 043820 (2012).